



Dispersive Elastic Moduli and Frequency-Dependent Attenuation due to Wave-Induced Fluid Flow in Metapelite

C. Fliedner *, M. E. French ¹

¹Department of Earth, Environmental and Planetary Sciences, Rice University, Houston, United States of America

Author contributions: *Conceptualization:* CF, MF. *Methodology:* CF. *Software:* CF. *Validation:* CF. *Formal Analysis:* CF. *Investigation:* CF. *Writing - original draft:* CF, MF. *Writing - Review & Editing:* CF, MF. *Visualization:* CF. *Supervision:* MF. *Funding acquisition:* CF, MF.

Abstract Seismic waves are used to interpret geologic structure, composition, and environmental conditions in the Earth. However, rocks are not perfectly elastic and their viscoelasticity dissipates energy during wave propagation. In saturated rocks, wave-induced fluid flow mechanisms can cause viscoelasticity resulting in frequency-dependent attenuation, velocities, and elastic moduli (dispersion). In subduction zones, some regions exhibit evidence of overpressurized fluids where dispersion and attenuation are hypothesized to be important in interpreting fault slip behavior from seismic waves. However, their importance has not been well-characterized because of a lack of measurements on relevant lithologies and under saturated conditions. We measured the Young's and shear moduli and the attenuation of a greenschist facies metapelite with the forced oscillation technique at frequencies between 2×10^{-5} and 30 Hz. The moduli and attenuation are frequency-dependent under saturated conditions and depend on effective pressure. At relatively low effective pressure, the Young's and shear moduli increase by over 50% between 2×10^{-5} and 30 Hz. We use Standard Linear Solid viscoelastic models to investigate the relationship between the attenuation and dispersion in the Orocopia schist. The models agree with the experimental data and demonstrate that viscoelasticity causes significant dispersion and attenuation in subduction zones, affecting our interpretation of earthquakes.

Non-technical summary Seismic waves from earthquakes are used to image and interpret the composition, structure, and environmental conditions of the Earth. Since rocks are not perfectly elastic, waves slow down and lose energy during propagation. The decrease in wave energy (i.e., attenuation) manifests as an amplitude reduction and velocity changes reflect changes in elastic moduli. Pore fluids cause both attenuation and changes in elastic moduli. To interpret fault slip with seismic waves, we must understand how they evolve as they reach the surface. Measurements of attenuation and elasticity relevant to fluid-rich areas in active subduction zones are limited but crucial. We conducted laboratory experiments on schist, common in subduction zones, to measure its attenuation and elasticity using the 'forced oscillation' method. Hence, we apply a cyclical force at a specific frequency, mimicking wave frequencies of earthquakes, and measure the induced deformation. We analyzed the amplitude and time difference between the force and the deformation to determine the rock properties. The properties vary with frequency and increase by over 50% when fluid content is high. Using physics models, we conclude that rock properties change because of fluid movement in the pores. Consequently, fluids significantly affect how we interpret rock properties in subduction zones.

Production Editor:
Garreth Funning
Handling Editor:
Pathikrit Bhattacharya
Copy & Layout Editor:
Ethan Williams

Signed reviewer(s):
David Healy, Nir Badt

Received:
27 March 2023
Accepted:
26 November 2023
Published:
26 January 2024

1 Introduction

Elastic waves are one of the most powerful tools for constraining processes in Earth's interior. They are used to image Earth's structure, interpret its composition and environmental conditions such as temperature and fluids, and constrain the physics of processes like fault slip. The amplitudes of elastic waves decay as they propagate away from their source (Anderson and Archambeau, 1964; Karato, 1993). This energy dissipation is called attenuation which results from viscoelastic deformation of the rock and is quantified using the quality factor Q (Anderson and Archambeau, 1964; Brennan and Stacey, 1977). In Earth's upper crust, attenuation ($1/Q$), occurs primarily due to fluid flow between pores and micro-

racks, which dissipates energy (O'Connell and Budiansky, 1974, 1977; Winkler and Nur, 1979; Bernabé and Revil, 1995; Borgomano et al., 2019). As a result of this energy dissipation, saturated rocks attenuate elastic waves and the elastic moduli and wave velocities depend on frequency, which is called dispersion (O'Connell and Budiansky, 1977; Winkler and Nur, 1979; Spencer, 1981). To make geologic interpretations on the basis of seismic velocities and attenuation, it is crucial to determine how they depend on wave frequency and to extrapolate them across geologic conditions requires determining the underlying processes that control attenuation and dispersion.

Because of the effects of water on wave propagation, attenuation and dispersion of elastic moduli may be significant in regions of subduction zones with high pore

*Corresponding author: celine.fliedner@rice.edu

pressure, although the rocks and conditions are not as well studied as those of the upper crust. Regions of anomalously low P-wave (V_P) and S-wave (V_S) velocities and high V_P/V_S are sometimes observed below the seismogenic zone of megathrusts where diverse modes of fault slip, including tremors, low-frequency earthquakes (LFEs), and very low-frequency earthquakes (VLFs) are also observed (Audet et al., 2009; Shelly et al., 2006; Bostock et al., 2012; Delph et al., 2018; Calvert et al., 2020). Field observations reveal the presence of low-porosity metapelite rocks rich in phyllosilicates, as well as extensive veining which supports the geophysical evidence of high pore pressure (Philippot and Selverstone, 1991; Angiboust et al., 2015; Muñoz-Montecinos et al., 2021; Condit and French, 2022). High pore pressure at these depths is thought to be caused by the release of water during dehydration reactions during greenschist to blueschist facies metamorphism (Peacock, 1987; Muñoz-Montecinos et al., 2021; Tewksbury-Christle et al., 2021; Condit et al., 2022). The dehydration of metabasalt and metapelite in particular, may release enough fluid to create high pore pressure at depths of slow slip and low-frequency events (Condit et al., 2020). However, although seismic imaging provides information that we use to infer fluid conditions at depth, we know little about how seismic waves are altered as they propagate through the rocks at these conditions.

Correlations between diverse modes of fault slip and evidence for high fluid pressure have resulted in the prominent hypothesis that fluid pressure somehow causes tremors, LFEs, and/or VLFs. An alternative hypothesis is that attenuation and dispersion caused by high pore fluid pressure alter the seismic waves of small typical earthquakes such that they appear as LFEs and/or VLFs by the time the waves are recorded at the surface (Gomberg et al., 2012; Bostock et al., 2017; Littel et al., 2018; Nakai et al., 2021). Specifically, the frequency range of typical earthquakes ranges from 1 to 30 Hz, but LFEs and VLFs are depleted in high frequencies and primarily exhibit wave frequencies between 0.1 and 8 Hz (Farge et al., 2020; Supino et al., 2020; Ide et al., 2007; Obara, 2002; Obara and Kato, 2016; Shelly et al., 2007; Thomas et al., 2016; Bostock et al., 2015). It is unclear if the low frequencies of these events are caused by attenuation of the waves or a slower rupture and slip mechanism at the source (Ito et al., 2007; Gomberg et al., 2016; Shapiro et al., 2018; Sammis and Bostock, 2021; Wei et al., 2021). We previously showed that overpressurized fluids can cause attenuation in the laboratory that is sufficient to deplete high frequencies during seismic wave propagation (Fliedner and French, 2023j). Here we use additional experimental data and rock physics models to quantitatively evaluate the mechanisms of attenuation and the magnitudes of velocity dispersion, and then extrapolate the results to in-situ conditions where LFEs and VLFs occur beneath the seismogenic zone.

Previous studies demonstrate that the elastic moduli of porous sedimentary rocks are dispersive at seismic frequencies (0.1 - 30 Hz) because of wave-induced fluid flow occurring in the pore space (Farge et al.,

2020; Ide et al., 2007; Obara, 2002; Obara and Kato, 2016; Thomas et al., 2016; Shelly et al., 2007; Supino et al., 2020). However, measurements of dispersion and attenuation on the lithologies present near the base of the subduction seismogenic zone are scarce (Fliedner and French, 2023j). The thin elongate pores characteristic of schists are particularly compressible under load (Walsh, 1965; Mavko and Nur, 1978; Kranz, 1983) and the small stress perturbations caused by propagating waves can close the pores and cause wave-induced fluid flow (White, 1975; Mavko and Nur, 1975; Pride et al., 2004), resulting in considerable attenuation (Toksöz et al., 1979; Gomberg et al., 2012; Fliedner and French, 2021, 2023j). Wave-induced fluid flow is often observed at seismic frequencies (Mavko and Nur, 1975; Dvorkin et al., 1994; Batzle et al., 2006), because fluid has time to flow between pores. In contrast, when the wave frequency is high (ultrasonic), fluid does not have enough time to flow and the rock properties are predicted to be independent of frequency (Biot, 1956; Toksöz et al., 1979). This is one reason elastic moduli measured in the laboratory tend to differ between ultrasonic and seismic frequencies (O'Connell and Budiansky, 1977; Adelinet et al., 2010; Dvorkin et al., 1994; Spencer, 1981; Pimienta et al., 2015; Borgomano et al., 2019). The fluid flow mechanisms that cause attenuation and dispersion at seismic frequencies and their relationship to the rock microstructure remain difficult to constrain from laboratory data and are rarely reported (Fliedner and French, 2023j). Fluid substitution models can predict elastic moduli at seismic frequencies, but they have yet to be confirmed by laboratory experiments for a number of lithologies, including metapelites (Gassmann, 1951; Brown and Korringa, 1975).

We present laboratory measurements of the frequency-dependent elastic moduli of a greenschist facies metapelite, the Orocopia schist, at frequencies between 2×10^{-5} and 30 Hz under dry and saturated conditions. This study is the first to report the elastic moduli and attenuation of phyllosilicate-rich metapelite under saturated conditions and at seismic frequencies. We combine these measurements with the attenuation measurements ($1/Q$) reported in (Fliedner and French, 2023j) to demonstrate that dispersion occurs concurrently with frequency-dependent attenuation. Together, these data allow us to apply rock physics models of wave-induced fluid flow and evaluate the mechanisms responsible. Using the Standard Linear Solid viscoelastic model, we show that the measured attenuation and dispersion in elastic moduli can be explained by the occurrence of two wave-induced flow mechanisms, squirt flow and patchy saturation. With this information and an understanding of the rock microstructure, it is then possible to make predictions about attenuation at geologic conditions under different fluid conditions.

2 Orocopia Schist

We collected a sample of the Orocopia schist from the Orocopia Mountains of Southern California (Figure 1a)

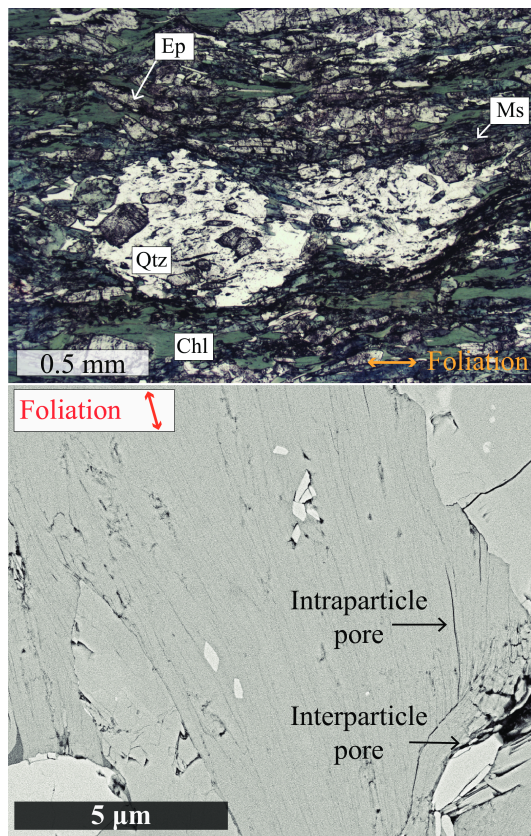


Figure 1 (a) A photomicrograph of a thin section of the Orocopia schist. Foliation is defined by aligned phyllosilicates and the orientation of individual minerals is indicated in pink. (b) Backscattered electron (BSE) images of the Orocopia schist. Foliation orientation is indicated with a red arrow. Pores are dominantly low aspect ratio (crack shaped) with the long axes parallel to the phyllosilicates and foliation plane. Figure from (Fliedner and French, 2021)

and the same block was used in the experiments of Fliedner and French (2021) and Fliedner and French (2023j). The Orocopia schist is a metapelite formed during Laramide subduction and reached peak conditions of 1.1 GPa pressure and 600 °C. However, it subsequently underwent greenschist facies metamorphism, which is reflected in its current mineral assemblage (Chapman et al., 2016; Jacobson and Dawson, 1995; Jacobson et al., 2007). The modal composition of our sample was reported in Fliedner and French (2021) and is 24% quartz, 31% chlorite, 22% muscovite, 17% epidote, and 3% calcite, similar to that reported in other studies of the Orocopia schist (Jacobson and Dawson, 1995; Jacobson et al., 2007; Platt et al., 2018). The schist has a well-defined foliation caused by the shape preferred orientation of phyllosilicate and quartz grains (Fliedner and French, 2021). The abundance of aligned phyllosilicates creates a primary transverse isotropic symmetry that we confirmed with ultrasonic velocity measurements and effective medium models (Fliedner and French, 2021). The sources of transverse isotropy can be seen in backscattered electron images which show phyllosilicate grains aligned within 5–10° and occasionally up to 25° to the foliation plane (Figure 1b). The schist

has a secondary transverse isotropy caused by abundant thin elongated pores oriented sub-parallel to phyllosilicate grains (Figure 1). Porosity includes delamination cracks, intragranular fractures, and both elongated and equant intergranular pores. The connected porosity is approximately 1 % and was determined in the laboratory using the difference between the mass of a water-saturated core of known volume and the mass of the same core under dry conditions. The permeability normal to the foliation is $4.2 \times 10^{-19} \text{ m}^2$ and was measured by CoreLaboratories using a steady state nanoporemeter under hydrostatic conditions at a pressure of 10 MPa and with nitrogen gas pore fluid at 0.2 MPa. Because our experiments were conducted with water pore fluid, not nitrogen, the water permeability may be lower due to the Klinkenberg effect which describes the slip of gases along pore walls (e.g., Tanikawa and Shimamoto (2009)). A precise correction requires a measurement of pore radii. However, previous research on rocks of similar gas permeability shows that the water permeability may be up to one order of magnitude lower, leading to a lower-bound water permeability of $\sim 4.2 \times 10^{-20} \text{ m}^2$ (Tanikawa and Shimamoto, 2009).

We measured the attenuation and elastic moduli of a single core of Orocopia schist to limit the effects of sample variability on our measurements. The core is oriented with its axis normal to foliation; this is the expected approximate orientation of wave travel away from the megathrust in subduction zones and the expected orientation of maximum attenuation, $1/Q$ (Delle Piane et al., 2014; Mikhaltsevitch et al., 2020). The experimental core has a diameter of 52.9 mm and a height of 25.4 mm. The core ends were trimmed and ground flat with a surface grinder. Prior to measurements under saturated conditions, the core was pre-saturated in deionized water under vacuum for seven days. In Fliedner and French (2021), we estimated the time scale of fluid diffusion in the Orocopia and determined that 12 hrs is sufficient as long as the water permeability is higher than $\sim 8 \times 10^{-22} \text{ m}^2$. Thus, 7 days should be sufficient to saturate most connected porosity, but it is possible that some gas remains trapped in disconnected pores or those connected by extremely small pore throats.

3 Methods

3.1 Experimental setup

Elastic moduli and attenuation measurements were made using a servo-controlled triaxial deformation apparatus at Rice University (Figure 2). In this apparatus, a silicone oil confining medium applies the least compressive stress (σ_3) parallel to the core radius and deionized water applies the pore fluid pressure (P_f) through the bottom end cap. The pore fluid outlet in the top end cap is closed, which prevents a dead volume of fluid that can create measurement artifacts (Dunn, 1986; Pimienta et al., 2016a). When accounting for the low porosity of the Orocopia schist and the experimental setup, dead volume is expected to have a negligible impact on our measurements (Dunn, 1986; Pimienta

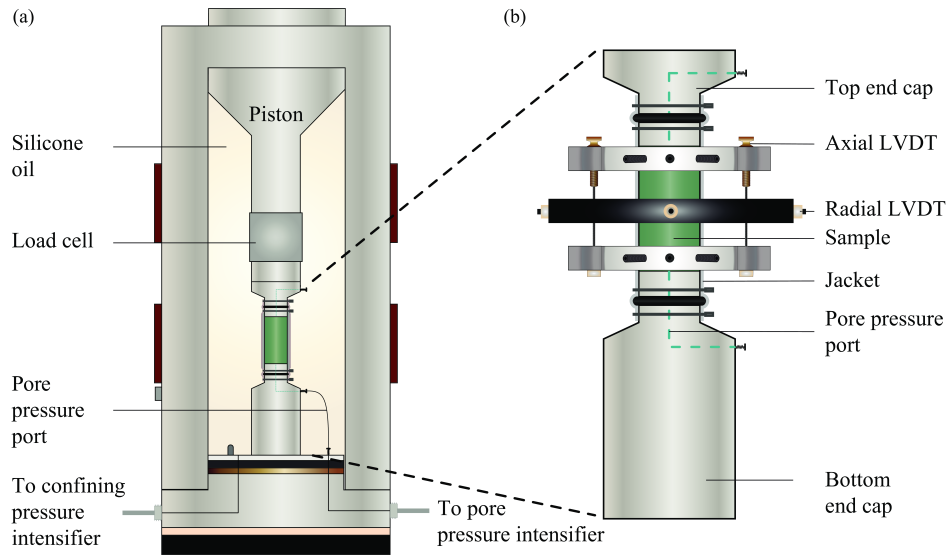


Figure 2 The triaxial deformation apparatus. (a) Diagram of the pressure vessel and (b) Magnified view of the sample configuration with the 2 axial LVDTs and 4 radial LVDTs.

et al., 2016a). The sample and pore fluid are isolated from the silicone oil with two polyolefin jackets (Figure 2b), which limits lateral fluid flow between the sample and the jackets. An axial piston applies the greatest compressive stress (σ_1) parallel to the core axis. The differential stress ($\sigma_1 - \sigma_3$) is recorded with an internal load cell having a precision of 0.3 MPa. Deformation of the sample is measured using 6 linear voltage differential transformers (LVDTs), 2 axial and 4 radial. The 2 axial LVDTs are placed at a 180° from one another and the 4 radial LVDTs are at a 90° from one another. Axial deformation was always measured with high resolution (63 nm) LVDTs and radial deformation was measured with high resolution LVDTs in 2 experiments and medium resolution (250 nm) LVDTs in 2 experiments (Table 1). The experiments were conducted at room temperature and temperature within the pressure vessel was measured. The internal temperature varied less than 1°C .

We used the forced oscillation technique to measure the frequency-dependent attenuation and elastic moduli of the Orocopia schist and 2 well-characterized materials, aluminum alloy (Al-6061) and Poly(methyl methacrylate) (PMMA), to calibrate our measurements (Figure 1a) (Spencer, 1981; Jackson and Paterson, 1987; Batzle et al., 2006). Measurements were made at frequencies between 2×10^{-5} and 30 Hz and the attenuation measurements of Orocopia schist were previously reported in Flidner and French (2023j). The forced oscillation technique consists of applying a small sinusoidal oscillation in stress at a discrete frequency parallel to the core axis and then measuring the induced axial and radial strains. Deformation is assumed to be anelastic, meaning completely recoverable but with some energy dissipation. Recoverable deformation is assumed because stress and strain are small, and our measurements evaluate if and how much energy is dissipated.

The Young's modulus, E is determined from the ratio of the amplitudes in stress (σ_a) and resulting axial strain

(ε_a):

$$E = \frac{\sigma_a}{\varepsilon_a} \quad (1)$$

The relationship between the different elastic moduli means that the shear modulus, which is defined as the ratio of shear stress to shear strain, can be determined from the Young's modulus (Equation 1) and the Poisson's ratio, ν . The Poisson's ratio is the ratio of the radial strain (ε_r) and axial strain ($\nu = -\varepsilon_r/\varepsilon_a$). The shear modulus can be determined from the axial stress and the difference between the axial and radial strain as:

$$G = \frac{E}{2(1 + \nu)} = \frac{\sigma_a}{2(\varepsilon_a - \varepsilon_r)} \quad (2)$$

The phase offset between the stress oscillation and the induced strain, ϕ , is measured in radians and gives the attenuation as $1/Q = \tan \phi$ at that frequency where Q is a property called the quality factor (Nowick and Berry, 1972). We measured the Young's modulus attenuation ($1/Q_E$) from the phase difference between the axial stress, σ_a , which has phase $\phi(\sigma_a)$, and axial strain, ε_a which has phase $\phi(\varepsilon_a)$:

$$1/Q_E = \tan(\phi(\sigma_a) - \phi(\varepsilon_a)) \quad (3)$$

The shear modulus attenuation (Q_S) is given by the phase difference between axial stress, σ_a , and the difference between axial strain (ε_a with phase $\phi(\varepsilon_a)$) and radial strain (ε_r with phase $\phi(\varepsilon_r)$) (Yin et al., 2019):

$$1/Q_S = \tan(\phi(\sigma_a) - \phi(\varepsilon_a - \varepsilon_r)) \quad (4)$$

We conducted two experiments on an aluminum core (G0188, G0198) and two experiments on PMMA (G0184, G0197) as summarized in Table 1 (Flidner and French, 2023a,f,c,g). Core dimensions for these samples are 50 mm in length and 25.4 mm in diameter. We reported the attenuation measurements for one experiment on dry Orocopia schist (G0187) and four experiments on water-saturated Orocopia schist at two different effective pressures (G0190, G0191, G0199, G0200) in Flidner

Set	Test	Sample	σ_3	P_f	P_{eff}	$\sigma_1 - \sigma_3$	A_{pp}	N_f	Frequency range	Radial LVDT?
			MPa	MPa	MPa	MPa	MPa		Hz	
1	G0184	PMMA	3	0	3	3	0.4	71	1×10^{-4} - 30	No
	G0187	Orocopia	10	0	10	10	1	71	1×10^{-4} - 30	No
	G0188	Al-6061	10	0	10	10	1	69	1×10^{-4} - 30	Yes
	G0190	Orocopia	10	1	9	10	1	73	1×10^{-4} - 30	Yes
	G0191	Orocopia	10	8	2	10	1	72	1×10^{-4} - 30	Yes
2	G0197	PMMA	10	0	5	5	1	80	1×10^{-4} - 30	Yes
	G0198	Al-6061	10	0	10	10	1	13	1×10^{-4} - 10	Yes
	G0199	Orocopia	10	1	9	10	1	57	2×10^{-5} - 10	Yes
	G0200	Orocopia	10	8	2	10	1	82	2×10^{-5} - 10	Yes

Table 1 Table of the forced oscillations experiments conducted. The experiments were conducted in two separate runs to establish reproducibility, each of which is labeled as a set. The environmental conditions are the confining pressure (σ_3), the pore pressure (P_f), the effective pressure (P_{eff}), the differential stress ($\sigma_1 - \sigma_3$), and the peak-to-peak amplitude (A_{pp}) of the sinusoidal stress oscillation. N_f is the total number of measurements made over all frequencies during a given test.

and French (2023j) and show those results here along with the elastic moduli from the same experiments, which are not reported elsewhere (Fliedner and French, 2023b,d,h,e,i). All measurements were made at a confining pressure of 10 MPa except for one experiment on PMMA, which was conducted at 5 MPa (G0197). Measurements made on the Orocopia schist under saturated conditions were made at 1 and 8 MPa pore fluid pressure, resulting in Terzaghi effective pressures ($P_{eff} = \sigma_3 - P_f$) of 9 and 2 MPa (Terzaghi et al., 1996).

For measurements under dry conditions, including on aluminum and PMMA, the confining pressure was increased by 1 MPa every 5 minutes until 10 MPa and the sample equilibrated at pressure for 12 hours. For measurements under saturated conditions, an initial confining pressure of 5 MPa and a pore pressure of 0.5 MPa were applied. Next, we increased the pore pressure to 1 MPa and confining pressure to 10 MPa over 10 minutes and allowed the system to equilibrate for 12 hours (G0190 and G0199). Following measurements at these conditions, we increased the pore pressure to 8 MPa over 10 minutes and again allowed the sample to equilibrate for 12 hours (G0191 and G0200). The two separate sets of experiments were made under saturated conditions to establish the reproducibility of our measurements.

Once at experimental conditions, we applied a small differential stress of 10 MPa to assure contact between the end caps and the sample and then applied a sinusoidal stress oscillation with a peak-to-peak amplitude of 1 MPa (0.4 MPa for one experiment on PMMA), which causes axial strains of $\sim 10^{-5}$. Measurements of elastic moduli and attenuation were made at 22 discrete frequencies from 1×10^{-4} to 30 Hz on aluminum and PMMA and at 26 discrete frequencies from 2×10^{-5} to 30 Hz on the Orocopia schist. The data sampling frequency varied between 50 and 5000 Hz and increased with the frequency of the stress oscillation. Multiple measurements were made at a given frequency during

an experiment and in total, we conducted between 2 and 6 forced oscillation tests at each frequency and effective stress. Experiments on the aluminum and PMMA cores we made in between the two sets of experiments made on the Orocopia schist to verify the accuracy and consistency of our measurements (Table S1 and Table S2).

3.2 Calibration

We corrected the attenuation and elastic moduli to account for signal distortion which is primarily caused by electronic noise at high frequencies and changes in environmental conditions like room temperature at low frequencies. We do so using the measurements of attenuation and elastic moduli on aluminum alloy (Al-6061) and Poly(methyl methacrylate) (PMMA), which are well-characterized (Figure 3). Aluminum has very low and frequency-independent attenuation and high elastic moduli (Lakes, 2009; Duffy, 2002; Oberg and McCauley, 2020) and PMMA has a relatively high frequency-dependent attenuation and low elastic moduli (Lakes, 2009; Madonna and Tisato, 2013; Saltiel et al., 2017; Lee et al., 2000). Radial deformation was recorded during both experiments on aluminum (G0188 and G0198), but a high-resolution LVDT was only used during one of the experiments (G0188, Table 1). Radial deformation was only measured during one of two experiments on PMMA (G0197), so we do not report shear modulus or Q_S for the other (G0184).

We calibrated the elastic moduli and the attenuation measurements using equations with 4 fitted parameters, A , B , C and D (Equation 5). Each parameter accounts for different effects, with A correcting for the effect of amplifiers and B and C correcting for phase distortion effects at high and low frequencies, respectively. The coefficient D corrects for effects independent of frequency. The parameters A , B , C and D were determined as the correction required to fit our measurements on aluminum and PMMA to the published

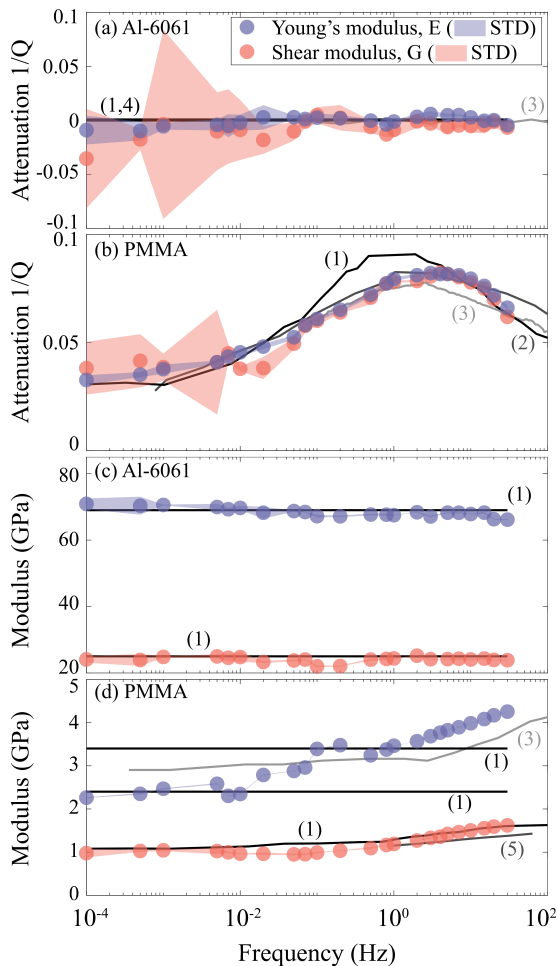


Figure 3 The results of calibration measurements on 6061 aluminum alloy (Al-6061) and Poly(methyl methacrylate) (PMMA) samples after correction using Equation 5. The Young's moduli and attenuation are shown in blue and shear moduli and attenuation are shown in pink. The blue and pink shaded areas indicate the standard deviation (STD) for the Young's and shear moduli measurements, respectively, and are extrapolated between point measurements. Published values of attenuation and elastic moduli are shown with grey lines for reference and labeled as (1) Young's and Shear moduli from Lakes (2009), (2) Shear modulus from Lee et al. (2000), (3) Young's modulus from Madonna and Tisato (2013), (4) Shear modulus from Duffy (2002), and (5) Shear modulus from Saltiel et al. (2017). (a) Attenuation $1/Q_E$ and $1/Q_S$ of Al-6061, (b) Attenuation $1/Q_E$ and $1/Q_S$ of PMMA, (c) Young's E and shear G moduli of Al-6061, and (d) Young's E and shear G moduli of PMMA.

references for these materials.

$$Data_{corrected} = A * data + B * f + C * \log_{10}(f) + D \quad (5)$$

We collected calibration data during each of the two sets of measurements (Table 1). During one set an additional amplifier was used, resulting in different values of A, B, C and D for the two sets (Figures S2 to S10 in Supplementary material). For the first group (G0184, G0187, G0190, and G0191), we first fit Equation 5 to aluminum so that it conforms to published values, and then applied the same correction to the experiments

on the PMMA to confirm that the corrected results are consistent with published values and then the Orocopia schist. For the second group, we fit Equation 5 to the PMMA (G0197) and the aluminum (G0198) separately to conform with published values. The Orocopia schist (G0199, G0200) was then corrected using the average parameters determined for PMMA (G0197) and Al-6061 (G0198). A table of the coefficients can be found in the Supplementary Materials (Tables S1 and Table S2).

4 Results for Elastic Moduli and Attenuation

Under water-saturated conditions, the Orocopia schist is stiffer at most frequencies and has higher attenuation at all frequencies than under dry conditions (Figure 4a and c). We also measure higher Young's and shear moduli and lower attenuation ($1/Q_E$ and $1/Q_S$) at an effective pressure of 9 MPa than at 2 MPa. In addition, whereas the elastic moduli and attenuation are independent of frequency under dry conditions, both vary with frequency under water-saturated conditions.

Under dry conditions, the Young's modulus, E , is 50 GPa (± 0.160) at all frequencies tested (Figure 4a). For comparison, the Young's modulus at ultrasonic frequencies (1×10^6 Hz), which we reported in Flidner and French (2021), is 51 GPa indicating relatively constant stiffness over 10 orders of magnitude in frequency (Figure 4a). Under saturated conditions, the Young's modulus increases with increasing frequency (Figure 4a). For instance, at $P_{eff} = 2$ MPa the Young's modulus increases from 41 GPa (± 2) to 67 GPa (± 1) with increasing frequency from 2×10^{-5} Hz to 30 Hz, and it appears to increase in two phases (Figure 4a). At $P_{eff} = 2$ MPa Young's modulus increases linearly in log space from 41 to 57 GPa between 2×10^{-5} and 1×10^{-3} Hz and is then relatively constant until ~ 0.1 Hz, when it again increases approximately linearly in log space. The Young's modulus increases similarly in two phases at 9 MPa effective pressure although the plateau from 1×10^{-3} to 0.1 Hz is less clear, and the modulus is consistently 3 GPa greater than at 2 MPa effective pressure. At effective pressures of 2 and 9 MPa, the Young's moduli are 5 and 8 % lower at 30 Hz than at ultrasonic frequencies (1×10^6 Hz), and this is consistent with extrapolating the frequency-dependence observed in our data an additional 5 orders of magnitude (Flidner and French, 2021). Similar to the Young's modulus, the shear modulus is also dispersive under water-saturated conditions between 2×10^{-5} and 30 Hz and we did not measure the shear modulus under dry conditions (Figure 4b). For instance, at 2 MPa effective pressure, the shear modulus increases from 14 GPa (± 3) to 25 GPa (± 1) at 2×10^{-5} to 30 Hz. At a given frequency, the shear modulus measured at $P_{eff} = 2$ MPa effective pressure is ~ 2 GPa lower than the shear modulus at 9 MPa. In contrast to the Young's modulus, the shear moduli are actually higher at 30 Hz than at 1×10^6 Hz indicating that these results cannot be directly extrapolated to ultrasonic frequencies (Flidner and French, 2021).

Under dry conditions, attenuation of the Young's

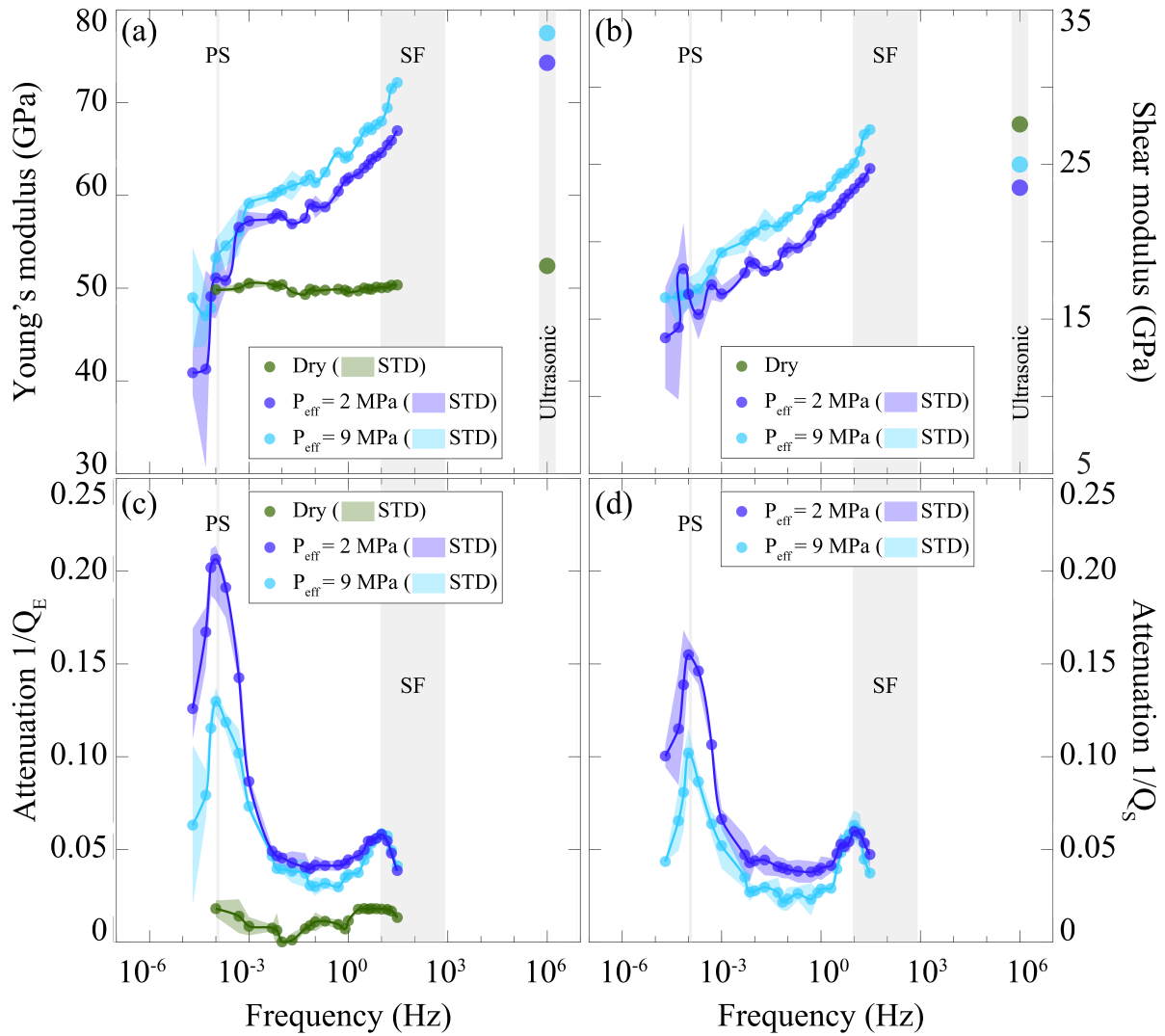


Figure 4 Results for attenuation and elastic moduli as a function of frequency for the Orocopia schist. Green markers indicate dry conditions at 10 MPa effective pressure, dark blue and light blue markers indicate saturated conditions at low (2 MPa) and high (9 MPa) effective pressures, respectively. Shading indicates the standard deviation (STD). The gray bars show the predicted characteristic frequencies for patchy saturation (PS) and squirt flow (SF) mechanisms at experimental conditions, which are described and analyzed in the discussion. (a) Young's modulus, E measured under dry and saturated conditions and compared to published moduli at ultrasonic frequency 1×10^6 Hz from Fliedner and French (2021). (b) Shear modulus G modulus measured under saturated conditions and compared to published moduli at ultrasonic frequency 1×10^6 Hz in Fliedner and French (2021), (c) Attenuation $1/Q_E$ measured under dry and saturated conditions, and (d) Attenuation $1/Q_S$ measured under saturated conditions.

modulus is $\sim 0.012 \pm 0.003$ at all frequencies tested (Figure 4c). In contrast, under saturated conditions, $1/Q_E$ is both higher than under dry conditions and dependent on frequency. For instance, at $P_{eff} = 2$ MPa, the minimum in $1/Q_E$ is $\sim 0.040 (\pm 0.001)$ between 0.02 and 0.5 Hz, which is about 4 times higher than attenuation under dry conditions. We measure two peaks in $1/Q_E$ under saturated conditions and these are centered at frequencies of 1×10^{-4} Hz and 10 Hz. In addition, the magnitude of $1/Q_E$ decreases with increasing effective pressure. For instance, the peak in attenuation ($1/Q_E$) at 1×10^{-4} Hz is ~ 0.210 at $P_{eff} = 2$ MPa, whereas it is ~ 0.130 at $P_{eff} = 9$ MPa. Similarly, the magnitude of $1/Q_S$ is frequency-dependent under saturated conditions and the attenuation is centered at the same frequencies (1×10^{-4} and 10 Hz) as for $1/Q_E$ (Fig-

ure 4d). At the 1×10^{-4} Hz peak, $1/Q_S$ is lower than $1/Q_E$ at the same peak by 0.053. At the higher frequency peak (10 Hz), the magnitudes of $1/Q_S$ and $1/Q_E$ are the same within the resolution of our measurements (1×10^{-3}). We observe a constant attenuation between 0.001 and 0.1 under saturated conditions, which corresponds to the frequency range over which the elastic moduli increase linearly. Shear modulus attenuation also decreases with increasing effective pressure, with $1/Q_S$ at an effective pressure of 2 MPa greater than at 9 MPa by 0.021 on average (Figure 4d).

5 Discussion

5.1 Wave-induced Fluid Flow

The presence of pore water and the magnitude of effective pressure both have a measurable effect on the elastic moduli and attenuation of the Orocopia schist. Relative to dry conditions, the attenuation under saturated conditions appears to be increased by a constant value (~ 0.003) with two superimposed frequency dependent peaks (Figure 4c). This constant increase in baseline attenuation is most clearly seen at frequencies between 2×10^{-2} and 3 Hz. As is the case for processes that result in near-constant attenuation, the elastic moduli also clearly increase near-linearly with frequency over this range (Figure 4) (Liu et al., 1976; Kjartansson, 1979). This background attenuation and linear increase in modulus do not arise from wave-induced fluid flow and are not evaluated in detail here.

Peaks in attenuation are frequently interpreted as being caused by wave-induced fluid flow in the rock. In our previous work, we showed that the patchy saturation and the squirt flow mechanisms are consistent with the positions of the peak in attenuation (Figure 4), although we did not evaluate their magnitude, which requires that we consider the dispersion of the elastic moduli (Flidner and French, 2023j).

The patchy saturation mechanism describes mesoscopic flow between two non-mixing fluids, such as air and water, coexisting in the pore network and forming heterogeneous saturation (White, 1975; Cleary, 1978; Schmitt et al., 1994; Pride et al., 2004). The characteristic frequency of the attenuation peak for patchy saturation (f_{patchy}) is (Cleary, 1978):

$$f_{patchy} = \frac{4kK_d}{\eta L^2} \quad (6)$$

where k is permeability, K_d is the drained bulk modulus, η is water viscosity, and L^2 is the length scale of saturation heterogeneity. In Flidner and French (2023j) we determined that the rock permeability must be $k \sim 1 \times 10^{-21} \text{ m}^2$ to explain the position of the peak at $1 \times 10^{-4} \text{ Hz}$ for a water viscosity of $10^{-3} \text{ Pa}\cdot\text{s}$, a drained bulk modulus of 61 GPa which we measured at 2.5 MPa effective pressure under dry conditions, and an assumed length scale of heterogeneous saturation equal to the sample length, $L \sim 53 \text{ mm}$. We assumed a constant water viscosity given the negligible temperature variation measured during the experiments. The estimated permeability ($1 \times 10^{-21} \text{ m}^2$) is 2 orders of magnitude lower than the permeability measured with a gas pore fluid ($4 \times 10^{-19} \text{ m}^2$) and 1 order of magnitude lower than the lower bound of permeability that we estimated by taking into account the Klinkenberg effect ($4 \times 10^{-20} \text{ m}^2$). This discrepancy may be attributed to the difference in the experimental conditions at which permeability and attenuation were measured. During the forced oscillations, there is an axial stress of 10 MPa, while the permeability was measured under isotropic stress conditions (Zoback and Byerlee, 1975). Thus, we conclude that the low frequency peak at $1 \times 10^{-4} \text{ Hz}$ is generally consistent with the patchy saturation mechanism due to air bubbles trapped in the low permeability pore network (White, 1975; Schmitt et al., 1994; Pride et al., 2004).

The squirt flow mechanism describes fluid flow oc-

curing at the pore scale from thin elongated pores into equant pores (Mavko and Nur, 1975; O'Connell and Budiansky, 1977; Dvorkin et al., 1994). Thin elongated pores are compressible and close with a small magnitude of applied stress whereas equant pores are much less compressible and remain open at the same stresses. Thus, when an elastic wave propagates through the rock, compliant pores close in response and fluid is pushed into the more equant pores (Mavko and Nur, 1975; Dvorkin et al., 1994). Pore geometry is described by the aspect ratio (α), where for an idealized ellipsoidal pore geometry α is the ratio between the short and long axes. The characteristic frequency of the attenuation peak for squirt flow (f_{squirt}) is (O'Connell and Budiansky, 1977):

$$f_{squirt} = \frac{K_s \alpha^3}{\eta} \quad (7)$$

where η is again the viscosity of water and K_s is the bulk modulus of the solid phase, absent pores. We estimated f_{squirt} from the viscosity of water $\eta = 10^{-3} \text{ Pa}\cdot\text{s}$ and our previous measurements on the Orocopia schist. We take the bulk modulus of the solid phase to be $K_s = 75 \text{ GPa}$, which we measured under dry conditions and at a confining pressure of 100 MPa, where most porosity is closed (Flidner and French, 2021, 2023j). We estimated the aspect ratio of the most compliant pore shape using

$$\alpha = \frac{2(1 - \nu^2)P_{clos}}{E_0} \quad (8)$$

(Mavko et al., 2020, therein Equation 2.10.71), where ν is Poisson's ratio, P_{clos} is the pressure required to close a pore with aspect ratio α and E_0 is the Young's modulus of the solid phase. For the Orocopia schist, we measured a Poisson's ratio of 0.25 and a Young's modulus of 81 GPa at a confining pressure of 100 MPa and under dry conditions. We can assume that the most compliant pores that are open at a given pressure are those just below their closure pressure P_{clos} . As a result, at effective pressures of 2 and 9 MPa, we find the most compliant pore shapes to be $\alpha \sim 4.5 \times 10^{-5}$ and $\alpha \sim 2.1 \times 10^{-4}$, respectively (Flidner and French, 2023j). If we use these aspect ratios in Equation 7, the resulting characteristic frequencies are 7.5 and 680 Hz for the peaks in attenuation at 2 and 9 MPa effective pressure (Flidner and French, 2023j). These predicted peaks are close to the position of the high frequency peak (10 Hz), particularly our estimate for 2 MPa effective pressure.

Although we show that the positions of the peaks in attenuation are generally consistent with the patchy saturation and squirt flow mechanisms, these are imprecise assessments of the mechanisms that control attenuation. We use viscoelastic models to assess whether the frequency-dependent attenuation and elastic moduli of the Orocopia schist can be quantitatively explained by the patchy saturation and squirt flow mechanisms.

5.2 Linear Viscoelastic Models

We employ models that assume the system consisting of the rock and pore fluid behaves as a viscoelastic material (O'Connell and Budiansky, 1977). The viscoelas-

ticity of the saturated rock arises from the combined viscous behavior of the fluid and the elastic behavior of the rock frame, assuming negligible viscous deformation of the mineral constituents. Numerically, the complex modulus $M^*(\omega)$ defines the anelastic modulus of a viscoelastic material with elastic (real part M') and viscous (imaginary part, M'') components as:

$$M^*(\omega) = M' + iM'' \quad (9)$$

We use the Maxwell representation of the Standard Linear Solid (SLS) model, also known as a Zener model, to investigate the causality between attenuation and dispersion in the Orocopia schist (Zener and Siegel, 1949). This model assumes a single viscous mechanism with viscosity η_0 , that dissipates energy in a short period of time. The mechanical behavior can be visualized using a circuit of springs to represent elastic deformation and dashpots to represent viscous deformation (Figure 5a). The Maxwell model consists of two parallel systems. The first is the Maxwell arm, which operates at the low-frequency limit and is composed of a spring of stiffness M_0 and a dashpot having the viscosity of the fluid, η_0 , connected in series. At the high-frequency limit, the undrained elastic modulus, M_∞ , controls the mechanical behavior of the rock since the fluid does not have enough time to flow. As a result, fluid viscosity has no effect on the mechanical behavior, and the second arm of the model is composed of a single spring. This model predicts that the attenuation ($1/Q$) has a Debye absorption peak centered at a characteristic relaxation time, τ_c . The characteristic relaxation time is the inverse of the characteristic angular frequency $\omega_c = 2\pi f_c$, with f_c being the characteristic frequency of the viscous mechanisms, in our case for either the patchy saturation (f_{patchy}) or squirt flow (f_{squirt}) mechanisms (Figure 5b). The elastic modulus, M' , increases with increasing angular frequency ω , from a low-frequency limit, M_0 , to a high-frequency limit, M_∞ . We use the formulation of the SLS model presented in (Mavko et al., 2020, therein Table 3.8.1):

$$M^*(\omega) = \frac{M_0 + iM_\infty \left(\frac{\omega}{\omega_c}\right)^2}{1 + \left(\frac{\omega}{\omega_c}\right)^2} \quad (10)$$

From the SLS model, $1/Q$ is determined as the ratio of the imaginary (M'') to real (M') parts of $M^*(\omega)$:

$$1/Q(\omega) = \frac{M''}{M'} = \tan(\phi) \quad (11)$$

The attenuation ($1/Q$) has a maximum magnitude that is proportional to the relaxation strength, Δ , which is the relative difference between the elastic moduli M_∞ and M_0 and occurs at a frequency ω_c :

$$1/Q_{max} = \frac{1}{2}\Delta = \frac{1}{2} \frac{M_\infty - M_0}{\sqrt{M_\infty M_0}} \quad (12)$$

with the relaxation strength given by (Lakes, 2009, Equation 2.50):

$$\Delta = \frac{M_\infty - M_0}{\sqrt{M_\infty M_0}} \quad (13)$$

(a) Standard Linear Solid (Maxwell)

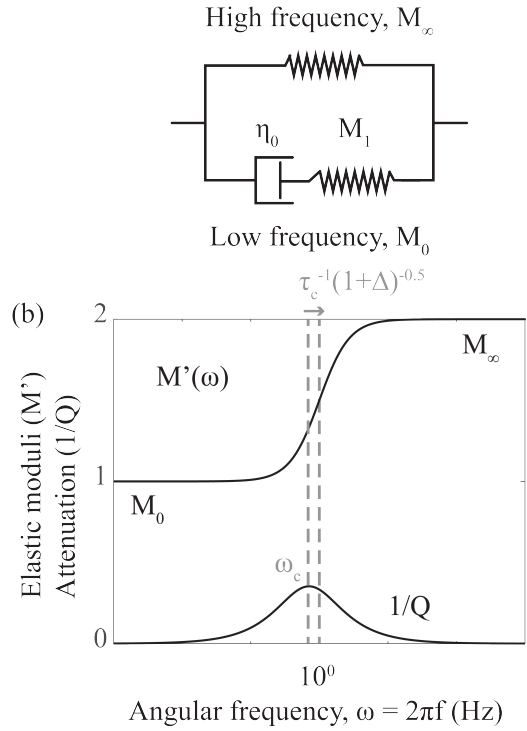


Figure 5 Diagram of the Maxwell representation of a Standard Linear Solid (SLS) model used to describe the viscoelastic behavior of the schist (a) The spring-dashpot analog of the SLS model with two systems in parallel. The first branch is a Maxwell solid that contains a spring (M_1) and a dashpot (η) in series, which represents the elastic and viscous components at the low-frequency limit. The first branch results in the viscoelastic deformation that occurs when there is fluid flow. The second branch is the elastic component at the high-frequency limit (M_∞) when no fluid flow occurs. (b) The SLS model predicts a non-linear increase in elastic moduli from M_0 at the low-frequency limit to M_∞ at the high-frequency limit. The increase in elastic moduli is centered at ω_c which is the characteristic angular frequency of the controlling fluid flow mechanism. The corresponding attenuation ($1/Q$) is a single Debye peak with an amplitude $1/Q_{max}$.

The increase in elastic modulus from the low to high frequency limits is centered near the peak in attenuation at ω_c but is shifted to higher frequencies by $1/(\tau_c \sqrt{1 + \Delta})$ (Figure 5b).

We estimated M_0 and M_∞ from our experimental measurements of elastic moduli and used the characteristic peak frequencies for patchy saturation and squirt flow (f_{patchy} and f_{squirt}) in Equation 10 to then calculate the attenuation of the Young's and shear moduli as a function of frequency using Equation 11. We evaluated the low and high frequency peaks separately by fitting the data separately over two frequency ranges from 5×10^{-5} to 2×10^{-2} Hz and 3 to 20 Hz corresponding to ranges over which we see peaks in attenuation above some background. The elastic moduli increase linearly between attenuation peaks (2×10^{-2} to 3 Hz), consis-

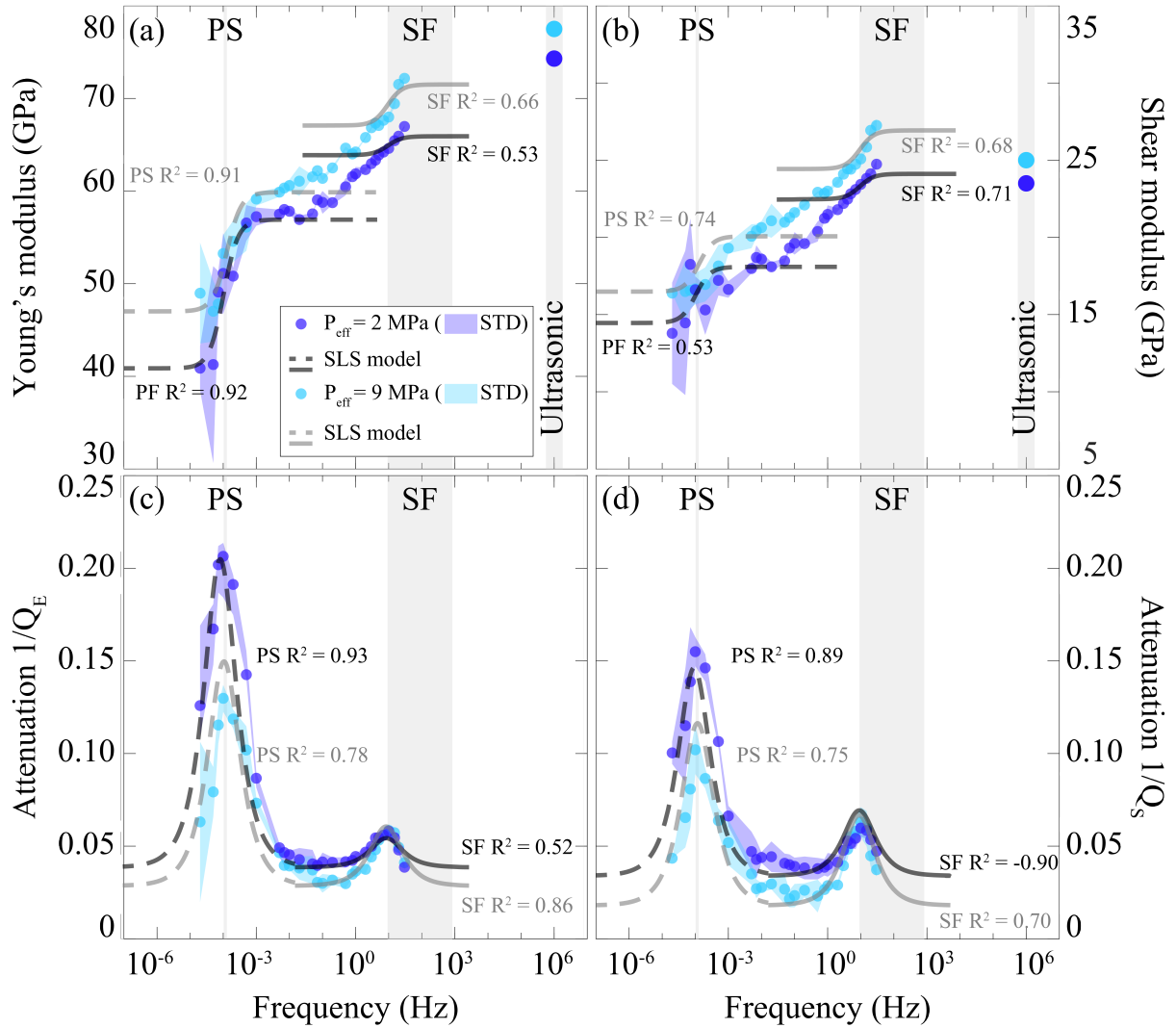


Figure 6 The measurements of frequency-dependent attenuation and elastic moduli under water-saturated conditions as shown in Figure 4 with the results of fitting the Standard Linear Solid (SLS) model to these experimental measurements. Dark blue and light blue colors indicate data at 2 and 9 MPa effective pressures, respectively. The dark and light gray lines indicate model results for the 2 and 9 MPa effective pressures. The model results for patchy saturation are shown with dashed lines and those for squirt flow are shown with solid lines. Gray bars show the predicted characteristic frequencies for the patchy saturation (PS) and squirt flow (SF) mechanisms at experimental conditions. (a) Young's modulus, E with previously reported moduli measured at ultrasonic frequency 1×10^6 Hz from [Fliedner and French \(2021\)](#), (b) shear modulus G with previously reported moduli measured at ultrasonic frequency 1×10^6 Hz from [Fliedner and French \(2021\)](#), (c) Attenuation $1/Q_E$, and (d) Attenuation $1/Q_S$. The goodness of fit of the SLS models to the experimental measurements of attenuation and elasticity were determined with a least square method and are shown, where a perfect fit occurs when R^2 equals 1.

tent with the near-constant attenuation at the same frequencies (Figure 6). Because the changes in elastic moduli due to wave-induced fluid flow are expected to be superimposed on this linear increase, we take M_0 and M_∞ to be the moduli at the low-frequency and high-frequency limits of each peak (Figure 6).

We find that the SLS model generally fits the attenuation data when parameterized with our measurements of elastic moduli and estimate of the peak positions for patchy saturation and squirt flow (Figure 6). Once we calculate attenuation as a function of frequency from Equation 11, we evaluate the goodness of fit between the model prediction and our data (Figure 6). Overall, the goodness of fit is best for the Young's modulus, lower effective pressure (higher fluid pressure), and the low-

frequency peak corresponding to patchy saturation. For instance, for the low-frequency peak and Young's modulus, R^2 was greater than 0.78 for both effective pressures (Figure 6a and c). The model for patchy saturation also fits our measurements of shear modulus with an R^2 of 0.53 and attenuation with an R^2 of 0.75 (Figure 6b and d). The goodness of fit of the SLS model to the experimental data is not as strong for the squirt flow mechanism as it is for the patchy saturation mechanism. At 9 MPa effective pressure, the model is in agreement with the measured Young's modulus and related attenuation ($R^2 > 0.58$), but the goodness of fit is poor for the shear modulus at $P_{eff} = 2$ MPa according to the coefficient of determination $R^2 < 0$. The lower quality of data resulting from lower resolution LVDTs and smaller strain in

the radial direction could explain the poor goodness of fit for the shear modulus attenuation. If we calculate the difference between the measured and model $1/Q_E$ at 10 Hz, we find a value of ~ 0.009 , consistent with previous attempts to fit SLS models to experimental data (Pimienta et al., 2016b, 2017; Borgomano et al., 2019; Sun et al., 2020).

Because of uncertainty in the aspect ratio of pores, predicting the attenuation and dispersion induced by squirt flow with the Standard Linear Solid model may cause some of the error in the fit. In previous studies of squirt flow, there are visual differences between model results and experimental data (Pimienta et al., 2016b, 2017; Borgomano et al., 2019; Sun et al., 2020), consistent with our relatively low coefficients of determination for the squirt flow mechanism, particularly at low effective stress (Figure 6). One contribution to error may be that the model considers only pores of a single aspect ratio, rather than a distribution of aspect ratios as may occur in rocks. Having a range of pore aspect ratios can cause a more complex squirt flow attenuation signal in a rock such as a broad peak spanning multiple frequencies (Anderson and Archambeau, 1964; Liu et al., 1976) or multiple distinct peaks at different characteristic frequencies (Anderson and Archambeau, 1964; Borgomano et al., 2019). Because we observed a single peak with a relatively narrow width, we used the squirt flow equation for a single aspect ratio. To directly measure the aspect ratio requires precise measurements of both pore diameter and length. Measurement of pore diameters is straightforward with porosimetry methods, but accurately assessing pore length is difficult due to a lack of reliable experimental techniques. Any errors in diameter or length measurement can significantly impact the predicted characteristic frequency of squirt flow because the aspect ratio is cubed in Equation 7. For example, A 10% margin of error in aspect ratio, gives α between 5.0×10^{-5} and 4.1×10^{-5} at 2 MPa effective pressure and results in a predicted range of characteristic frequencies of 5 and 9 Hz.

5.3 Controls of lithology on attenuation and dispersion

This paper is the first to quantify the attenuation and dispersion of a schist, to the best of our knowledge (Subramaniyan et al., 2014; Rorheim, 2022). We compare our results to other lithologies for which data are available, such as shales (Mikhaltsevitch et al., 2020; Delle Piane et al., 2014), sandstones (Pimienta et al., 2015, 2016b, 2017, 2021; Borgomano et al., 2020; Tisato and Madonna, 2012; Tisato et al., 2015; Madonna and Tisato, 2013), and limestones (Borgomano et al., 2017, 2019). To understand how viscoelasticity is controlled by patchy saturation and squirt flow mechanisms, we discuss the similarities between the rocks, including the relative permeability and pore geometry (Pimienta et al., 2021; Brace, 1977).

Reports of energy dissipation due to patchy saturation are most common in rocks with low permeability and thin elongated pores despite large differences in reported elastic moduli (Pimienta et al., 2021; Cleary,

1978; White, 1975). We find the characteristic frequency f_{patchy} for the Orocopia schist ($\sim 1 \times 10^{-4}$ Hz) to be similar to the predicted characteristic frequency for the Goldwyer shale (2×10^{-4} Hz) (Delle Piane et al., 2014). The Orocopia schist and Goldwyer shale have a similar estimated water permeability ($\sim 10^{-21}$ m²) and sheet silicate content ($>50\%$) (Delle Piane et al., 2014; Flidner and French, 2023j). In some rocks, patchy saturation is also estimated to be important at higher frequencies than we observe, with a f_{patchy} of 40 Hz for a different shale (Mikhaltsevitch et al., 2020) and ~ 300 Hz for a limestone (Borgomano et al., 2017), which are also lithologies with abundant elongated pores. Since both the Orocopia schist and Goldwyer shale have low permeability and small pore throats, bubbles of air can become trapped in their pore network (Pride et al., 2004). When a pressure wave is propagating through, the non-mixing air bubbles flow through the pores due to capillary forces (Schmitt et al., 1994; Delle Piane et al., 2014; Tisato et al., 2015). Thus, the occurrence of non-mixing patches of fluids may be more common in rocks rich in sheet silicates and thin elongated pores than other lithologies (Cleary, 1978; O'Connell and Budiansky, 1977). However, the magnitudes of the attenuation peak in the Orocopia schist and limestone ($1/Q_E > 0.13$ in Figure 4) are more than double the attenuation peak in the Goldwyer shale ($1/Q_E < 0.07$) (Borgomano et al., 2017; Delle Piane et al., 2014; Mikhaltsevitch et al., 2020). This might be caused by differences in the relaxation strength (Equation 13) which links the difference in the Young's modulus and energy dissipation and is consistent with the nearly one order of magnitude difference in elastic moduli between the Goldwyer shale (<7 GPa) and the Orocopia schist (50 GPa) (Figure 6a). Comparisons between experimental data and models that predict attenuation magnitude due to patchy saturation are not common. However, the agreement that we see between experimental data and the model ($R^2 > 0.78$ in Figure 6a and c) has also been observed in limestone (Borgomano et al., 2017).

The squirt flow mechanism is also a relatively common mechanism of attenuation, particularly in rocks with thin elongated pores. Squirt flow has been interpreted as occurring in several sandstones (Tisato and Madonna, 2012; Madonna and Tisato, 2013; Pimienta et al., 2015, 2017; Subramaniyan et al., 2015; Sun et al., 2020), as well as a thermally cracked limestone (Borgomano et al., 2019), and the frequency of the attenuation peak is strongly dependent on pore shape. The attenuation peak for squirt flow occurs at 10 Hz in the Orocopia schist and most sandstones display this peak between 0.1 and 300 Hz (Pimienta et al., 2017; Borgomano et al., 2019; Subramaniyan et al., 2015; Sun et al., 2020), although it can occur above 1000 Hz due to the typically higher aspect ratio pores in sandstones (Pimienta et al., 2016b; Tisato and Madonna, 2012; Yin et al., 2019). Because of the strong dependence on aspect ratio (Equation 7), the squirt flow mechanism is typically identified when α is $\sim 10^{-4}$ or smaller (Pimienta et al., 2017; Borgomano et al., 2019; Subramaniyan et al., 2015; Sun et al., 2020; Flidner and French, 2023j). To emphasize the necessity of thin elongated pores even further,

Borgomano et al. (2019) only observed evidence of the squirt flow mechanism in limestone after it had been thermally cracked. Despite the fact that both modeling and experimental studies underscore the necessity of elongated pores for squirt flow (Adelinet et al., 2011; Pimienta et al., 2016b), the lack of measurements on schist meant that it was previously unknown whether squirt flow occurs in these rocks at frequencies below 100 Hz (Delle Piane et al., 2014; Mikhaltsevitch et al., 2020).

Rocks rich in phyllosilicates have unique properties that enhance attenuation and dispersion through their influence on microstructure. For instance, rocks rich in phyllosilicates like the Orocopia schist often have a strong shape preferred orientation of grains that then leads to thin and elongated pores aligned with the foliation (Flidner and French, 2021). As a result, both the permeability and aspect ratios are impacted by the presence of phyllosilicates resulting in high compressibility normal to foliation and high attenuation and dispersion. In addition, phyllosilicate-rich rocks often have weaker fracture strength along their cleavage planes and parallel to foliation, which can cause additional microfracture and macrofracture porosity (Escartín et al., 1997). These macroscopic fractures have a similar shape to thin elongated pores and may cause additional attenuation and dispersion. Specifically, higher microfracture densities adjacent to faults or the presence of larger fractures that are not sampled at the laboratory scale may increase the magnitude of attenuation or cause an additional attenuation peak. Thus, our measurements can be considered a lower bound on the natural system.

5.4 Dispersive seismic velocities and attenuation in subduction zones

Because seismic tomography is the primary tool used to infer potential pore fluid overpressure along the subduction plate boundary, we use our results to evaluate tomographic evidence for fluid pressurization at depths of 25–40 km. In several subduction zones, these depths coincide with regions of low wave velocities, with P-wave velocities (V_P) of 5.0–6.5 km/s and S-wave velocities (V_S) of 2.0–3.2 km/s, and of high V_P/V_S of 2.0–2.8 (Audet et al., 2009; Calvert et al., 2011, 2020; Delph et al., 2018). To compare our results with tomography, we calculate the wave velocities from our measurements of the elastic moduli (Figure 4). The P-wave velocity is determined as $V_P \sim \sqrt{C_{33}/\rho}$ and the S-wave velocity as $V_S \sim \sqrt{G/\rho}$ where C_{33} is the stiffness normal to foliation, G the shear modulus (Figure 4), and ρ the density of the Orocopia schist determined in Flidner and French (2021). For the Orocopia schist, the Young's modulus normal to the foliation is 30 % lower than C_{33} at an effective pressure of ~ 2 MPa (Flidner and French, 2021). At a frequency of 1 Hz and an effective pressure of 2 MPa, the Young's modulus is 62 GPa resulting in C_{33} of 81 GPa and the shear modulus is 22 GPa (Figure 4). The resulting estimates of P-wave and S-wave velocities are $V_P \sim 5.2$ km/s and $V_S \sim 2.7$ km/s and their ratio is $V_P/V_S \sim 1.9$. Thus, our approxi-

mated velocities at low effective pressure conditions are consistent with the low velocities and high V_P/V_S observed in seismic tomography at 20–45 km in subduction zones (Audet et al., 2009; Calvert et al., 2011, 2020; Delph et al., 2018). We infer that pore fluid overpressurization in metapelites adjacent to the megathrust is consistent with the interpretations of seismic tomography and that the in-situ velocities are most likely dispersive.

Application of our attenuation results requires consideration of differences in laboratory and geologic conditions. Under water saturated conditions, measurements of attenuation are significant, with $1/Q_E$ consistently greater than 0.03. As evaluated in (Flidner and French, 2023j), the primary consideration when extrapolating to geologic conditions is the effect of fluid viscosity on the positions of the attenuation peaks (Equations 6 and 7). As depth increases, water viscosity decreases from 1×10^{-3} Pa·s at the near-surface to 1×10^{-4} Pa·s at 500 °C (Audet and Keppler, 2004). When peak position is adjusted to account for the supercritical nature of water at depths of 25–40 km, this increases the characteristic frequencies of wave-induced flow mechanisms (Flidner and French, 2023j). The adjusted peaks in $1/Q_E$ and $1/Q_S$ for squirt flow coincide with the range of depleted frequencies seen in low-frequency earthquakes (2–8 Hz to 30 Hz) (Farge et al., 2020; Supino et al., 2020) and part of the range of characteristic frequencies observed in very low-frequency earthquakes (0.1 Hz - 30 Hz) (Obana and Kodaira, 2009). In addition, the magnitude of attenuation at these frequencies is sufficient to cause the depletion of these high-frequency waves. While we predict that squirt flow impacts seismic waves significantly, patchy saturation is unlikely unless the permeability is higher at geologic conditions. We estimate the permeability that would be required for the characteristic frequency of patchy saturation to fall within the seismic frequency range (0.1 to 30 Hz). If we assume a bulk modulus similar to Orocopia schist and supercritical water viscosity at in-situ conditions, Equation 6 indicates that a permeability of 1×10^{-19} to 1×10^{-17} m² would be necessary to shift the peak to seismic frequencies. These values are high but not implausible for metamorphic rocks, and potentially could result from microfracture damage (Johnson, 1983; Katayama et al., 2012). As a result, models show that our laboratory measurements of attenuation due to squirt flow can explain the limited frequency range of earthquakes (Flidner and French, 2023j).

We evaluated the role of fluid viscosity on attenuation at geologic conditions, but lithology is likely an important control on the importance of attenuation and dispersion as well. For instance, in warm subduction zones the megathrust typically passes through greenschist facies, whereas cold subduction zones pass through blueschist and eclogite facies (Condit et al., 2020). Thus, although metapelites will undergo some metamorphism, they are expected to be phyllosilicate rich even along colder subduction paths. As we documented for the Orocopia schist, pore structure which is largely controlled by aligned phyllosilicates is the strongest control on bulk rock compliance and attenuation. Thus, although constraining the importance of

lithology on attenuation and dispersion would require additional laboratory measurements and microstructural observations of blueschist facies metapelites, we do not predict significant differences in the viscoelastic properties at seismic frequencies.

6 Conclusions

We used the forced oscillation technique to measure the dispersion of elastic moduli in the Orocopia schist at seismic frequencies (2×10^{-5} - 30 Hz) and then used our previous measurements of attenuation and Standard Linear Solid models to evaluate the mechanisms that control attenuation and dispersion. We find that the Young's and shear moduli are dispersive and the magnitudes depend on both water saturation and effective pressure. The Standard Linear Solid models fit the experimental data well and demonstrate that the dispersion is exclusively related to two peaks in attenuation controlled by wave-induced fluid flow. In addition, we show that the patchy saturation and the squirt flow mechanisms of attenuation and dispersion can be described using a single permeability and a single pore geometry, despite the complex microstructure of a schist. In both the schist and other lithologies, the predominance of thin elongated pores is the primary microstructural characteristic controlling the magnitude of dispersion. As a result, attenuation and dispersion are significant and can be modeled for geologic conditions in subduction zones where lithologies rich in phyllosilicates are present.

Acknowledgements

We would like to express our gratitude to our three reviewers: Dave Healy, Nir Badt, and an anonymous reviewer, for their time and effort in reviewing the manuscript. Their valuable comments and suggestions have greatly improved the quality of the manuscript. This research project has been funded by ACS-PRF grant 59440-DN18 to MF and by the David Worthington Named Grant from the AAPG Foundation Grants-In-Aid program to CF.

Data and code availability

The data are available on Zenodo at the following links:

- <https://doi.org/10.5281/zenodo.7545104>
- <https://doi.org/10.5281/zenodo.7545133>
- <https://doi.org/10.5281/zenodo.7545137>
- <https://doi.org/10.5281/zenodo.7545181>
- <https://doi.org/10.5281/zenodo.7528910>
- <https://doi.org/10.5281/zenodo.7529047>
- <https://doi.org/10.5281/zenodo.7529147>
- <https://doi.org/10.5281/zenodo.7529120>
- <https://doi.org/10.5281/zenodo.7529179>

Competing interests

The authors declare no conflict of interest.

References

- Adelinet, M., Fortin, J., Guéguen, Y., Schubnel, A., and Geoffroy, L. Frequency and fluid effects on elastic properties of basalt: Experimental investigations. *Geophysical Research Letters*, 37(2): n/a–n/a, 2010. doi: [10.1029/2009gl041660](https://doi.org/10.1029/2009gl041660).
- Adelinet, M., Fortin, J., and Guéguen, Y. Dispersion of elastic moduli in a porous-cracked rock: Theoretical predictions for squirt-flow. *Tectonophysics*, 503(1-2):173–181, 2011. doi: [10.1016/j.tecto.2010.10.012](https://doi.org/10.1016/j.tecto.2010.10.012).
- Anderson, D. L. and Archambeau, C. The anelasticity of the earth. *Journal of Geophysical Research*, 69(10):2071–2084, 1964.
- Angiboust, S., Kirsch, J., Oncken, O., Glodny, J., Monié, P., and Rybacki, E. Probing the transition between seismically coupled and decoupled segments along an ancient subduction interface. *Geochemistry, Geophysics, Geosystems*, 16(6):1905–1922, 2015. doi: [10.1002/2015gc005776](https://doi.org/10.1002/2015gc005776).
- Audet, P., Bostock, M. G., Christensen, N. I., and Peacock, S. M. Seismic evidence for overpressured subducted oceanic crust and megathrust fault sealing. *Nature*, 457(7225):76–8, 2009. doi: [10.1038/nature07650](https://doi.org/10.1038/nature07650).
- Audet, A. and Keppler, H. Viscosity of fluids in subduction zones. *Science*, 303(5657):513–6, 2004. doi: [10.1126/science.1092282](https://doi.org/10.1126/science.1092282).
- Batzle, M. L., Han, D.-H., and Hofmann, R. Fluid mobility and frequency-dependent seismic velocity — Direct measurements. *Geophysics*, 71(1):N1–N9, 2006. doi: [10.1190/1.2159053](https://doi.org/10.1190/1.2159053).
- Bernabé, Y. and Revil, A. Pore-scale heterogeneity, energy dissipation and the transport properties of rocks. *Geophysical Research Letters*, 22(12):1529–1532, 1995. doi: <https://doi.org/10.1029/95GL01418>.
- Biot, M. A. Theory of Propagation of Elastic Waves in a Fluid-Saturated Porous Solid. II. Higher Frequency Range. *The Journal of the Acoustical Society of America*, 28(2):179–191, 1956. doi: [10.1121/1.1908241](https://doi.org/10.1121/1.1908241).
- Borgomano, J. V. M., Pimienta, L., Fortin, J., and Guéguen, Y. Dispersion and attenuation measurements of the elastic moduli of a dual-porosity limestone. *Journal of Geophysical Research: Solid Earth*, 122(4):2690–2711, 2017. doi: [10.1002/2016jb013816](https://doi.org/10.1002/2016jb013816).
- Borgomano, J. V. M., Pimienta, L. X., Fortin, J., and Guéguen, Y. Seismic Dispersion and Attenuation in Fluid-Saturated Carbonate Rocks: Effect of Microstructure and Pressure. *Journal of Geophysical Research: Solid Earth*, 124(12):12498–12522, 2019. doi: [10.1029/2019jb018434](https://doi.org/10.1029/2019jb018434).
- Borgomano, J. V. M., Gallagher, A., Sun, C., and Fortin, J. An apparatus to measure elastic dispersion and attenuation using hydrostatic- and axial-stress oscillations under undrained conditions. *Rev Sci Instrum*, 91(3):034502, 2020. doi: [10.1063/1.5136329](https://doi.org/10.1063/1.5136329).
- Bostock, M. G., Royer, A. A., Hearn, E. H., and Peacock, S. M. Low frequency earthquakes below southern Vancouver Island. *Geochemistry, Geophysics, Geosystems*, 13(11), 2012. doi: [10.1029/2012gc004391](https://doi.org/10.1029/2012gc004391).
- Bostock, M. G., Thomas, A. M., Savard, G., Chuang, L., and Rubin, A. M. Magnitudes and moment-duration scaling of low-frequency earthquakes beneath southern Vancouver Island. *Journal of Geophysical Research: Solid Earth*, 120(9):6329–6350, 2015. doi: [10.1002/2015jb012195](https://doi.org/10.1002/2015jb012195).
- Bostock, M. G., Thomas, A. M., Rubin, A. M., and Christensen, N. I.

- On corner frequencies, attenuation, and low-frequency earthquakes. *Journal of Geophysical Research: Solid Earth*, 122(1): 543–557, 2017. doi: 10.1002/2016jb013405.
- Brace, W. F. Permeability from resistivity and pore shape. *Journal of Geophysical Research*, 82(23):3343–3349, 1977. doi: 10.1029/JB082i023p03343.
- Brennan, B. J. and Stacey, F. D. Frequency dependence of elasticity of rock—test of seismic velocity dispersion. *Nature*, 268(5617): 220–222, 1977. doi: 10.1038/268220a0.
- Brown, R. J. S. and Korringa, J. On the Dependence of the Elastic Properties of a Porous Rock on the Compressibility of the Pore Fluid. *Geophysics*, 40(4):608–616, 1975. doi: 10.1190/1.1440551.
- Calvert, A. J., Preston, L. A., and Farahbod, A. M. Sedimentary underplating at the Cascadia mantle-wedge corner revealed by seismic imaging. *Nature Geoscience*, 4(8):545–548, 2011. doi: 10.1038/ngeo1195.
- Calvert, A. J., Bostock, M. G., Savard, G., and Unsworth, M. J. Cascadia low frequency earthquakes at the base of an overpressured subduction shear zone. *Nat Commun*, 11(1):3874, 2020. doi: 10.1038/s41467-020-17609-3.
- Chapman, S., Tisato, N., Quintal, B., and Holliger, K. Seismic attenuation in partially saturated Berea sandstone submitted to a range of confining pressures. *Journal of Geophysical Research: Solid Earth*, 121(3):1664–1676, 2016. doi: 10.1002/2015jb012575.
- Cleary, M. P. Elastic and dynamic response regimes of fluid-impregnated solids with diverse microstructures. *International Journal of Solids and Structures*, 14(10):795–819, 1978. doi: 10.1016/0020-7683(78)90072-0.
- Condit, C. B. and French, M. E. Geologic Evidence of Lithostatic Pore Fluid Pressures at the Base of the Subduction Seismogenic Zone. *Geophysical Research Letters*, 49(12), 2022. doi: 10.1029/2022gl098862.
- Condit, C. B., Guevara, V. E., Delph, J. R., and French, M. E. Slab dehydration in warm subduction zones at depths of episodic slip and tremor. *Earth and Planetary Science Letters*, 552, 2020. doi: 10.1016/j.epsl.2020.116601.
- Condit, C. B., French, M. E., Hayles, J. A., Yeung, L. Y., Chin, E. J., and Lee, C. A. Rheology of Metasedimentary Rocks at the Base of the Subduction Seismogenic Zone. *Geochemistry, Geophysics, Geosystems*, 23(2), 2022. doi: 10.1029/2021gc010194.
- Delle Piane, C., Sarout, J., Madonna, C., Saenger, E. H., Dewhurst, D. N., and Raven, M. Frequency-dependent seismic attenuation in shales: experimental results and theoretical analysis. *Geophysical Journal International*, 198(1):504–515, 2014. doi: 10.1093/gji/ggu148.
- Delph, J. R., Levander, A., and Niu, F. Fluid Controls on the Heterogeneous Seismic Characteristics of the Cascadia Margin. *Geophysical Research Letters*, 45(20), 2018. doi: 10.1029/2018gl079518.
- Duffy, W. Acoustic quality factor of aluminium and selected aluminium alloys from 50 mK to 300 K. *Cryogenics*, 42(3-4): 245–251, 2002. doi: 10.1016/s0011-2275(02)00021-8.
- Dunn, K. Acoustic attenuation in fluid-saturated porous cylinders at low frequencies. *The Journal of the Acoustical Society of America*, 79(6):1709–1721, 1986. doi: 10.1121/1.393232.
- Dvorkin, J., Nolen-Hoeksema, R., and Nur, A. The squirt-flow mechanism: Macroscopic description. *Geophysics*, 59(3): 428–438, 1994. doi: 10.1190/1.1443605.
- Escartín, J., Hirth, G., and Evans, B. Nondilatant brittle deformation of serpentinites: Implications for Mohr-Coulomb theory and the strength of faults. *Journal of Geophysical Research: Solid Earth*, 102(B2):2897–2913, 1997. doi: 10.1029/96jb02792.
- Farge, G., Shapiro, N. M., and Frank, W. B. Moment-Duration Scaling of Low-Frequency Earthquakes in Guerrero, Mexico. *Journal of Geophysical Research: Solid Earth*, 125(8), 2020. doi: 10.1029/2019jb019099.
- Fliedner, C. and French, M. Forced Oscillations On PMMA (1). <https://doi.org/10.5281/zenodo.7545104>, 2023a.
- Fliedner, C. and French, M. Forced Oscillations On The Orocochia Schist Under Dry Conditions. <https://doi.org/10.5281/zenodo.7528910>, 2023b.
- Fliedner, C. and French, M. Forced Oscillations On Aluminum (1). <https://doi.org/10.5281/zenodo.7545133>, 2023c.
- Fliedner, C. and French, M. Forced Oscillations On The Orocochia Schist Under Saturated Conditions (Effective Stress 9 MPa) (1). <https://doi.org/10.5281/zenodo.7529047>, 2023d.
- Fliedner, C. and French, M. Forced Oscillations On The Orocochia Schist Under Saturated Conditions (Effective Stress 2 MPa) (1). <https://doi.org/10.5281/zenodo.7529120>, 2023e.
- Fliedner, C. and French, M. Forced Oscillations On PMMA (2). <https://doi.org/10.5281/zenodo.7545137>, 2023f.
- Fliedner, C. and French, M. Forced Oscillations On Aluminum (2). <https://doi.org/10.5281/zenodo.7545181>, 2023g.
- Fliedner, C. and French, M. Forced Oscillations On The Orocochia Schist Under Saturated Conditions (Effective Stress 9 MPa) (2). <https://doi.org/10.5281/zenodo.7529147>, 2023h.
- Fliedner, C. and French, M. Forced Oscillations On The Orocochia Schist Under Saturated Conditions (Effective Stress 2 MPa) (2). <https://doi.org/10.5281/zenodo.7529179>, 2023i.
- Fliedner, C. and French, M. E. Pore and Mineral Fabrics Control the Elastic Wave Velocities of Metapelite With Implications for Subduction Zone Tomography. *Journal of Geophysical Research: Solid Earth*, 126(10), 2021. doi: 10.1029/2021jb022361.
- Fliedner, C. and French, M. E. Measurements of wave-induced attenuation in saturated metapelite and the band-limitation of low-frequency earthquakes. *AGU Advances*, 4(2), 2023j. doi: 10.1029/2022AV000837.
- Gassmann, F. Über die Elastizität poröser Medien. *Vierteljahrsschrift der Naturforschenden Gesellschaft in Zürich. GEOPHYSICS*, 96:1–23, 1951.
- Gomberg, J., Creager, K., Sweet, J., Vidale, J., Ghosh, A., and Hotovec, A. Earthquake spectra and near-source attenuation in the Cascadia subduction zone. *Journal of Geophysical Research: Solid Earth*, 117(B5):n/a–n/a, 2012. doi: 10.1029/2011jb009055.
- Gomberg, J., Agnew, D. C., and Schwartz, S. Y. Alternative source models of very low frequency events. *Journal of Geophysical Research: Solid Earth*, 121(9):6722–6740, 2016. doi: 10.1002/2016jb013001.
- Ide, S., Beroza, G. C., Shelly, D. R., and Uchide, T. A scaling law for slow earthquakes. *Nature*, 447(7140):76–79, 2007. doi: 10.1038/nature05780.
- Ito, Y., Obara, K., Shiomi, K., Sekine, S., and Hirose, H. Slow earthquakes coincident with episodic tremors and slow slip events. *Science*, 315(5811):503–6, 2007. doi: 10.1126/science.1134454.
- Jackson, I. and Paterson, M. S. Shear modulus and internal friction of calcite rocks at seismic frequencies: pressure, frequency and grain size dependence. *Physics of the Earth and Planetary Interiors*, 45(4):349–367, 1987. doi: 10.1016/0031-9201(87)90042-2.
- Jacobson, C. E. and Dawson, M. R. Structural and metamorphic evolution of the Orocochia Schist and related rocks, southern California: Evidence for late movement on the Orocochia fault. *Tectonics*, 14(4):933–944, 1995. doi: 10.1029/95tc01446.
- Jacobson, C. E., Grove, M., Vučić, A., Pedrick, J. N., and Ebert, K. A. *Exhumation of the Orocochia Schist and associated rocks of south-*

- eastern California: Relative roles of erosion, synsubduction tectonic denudation, and middle Cenozoic extension, volume 419, book section 1, pages 1–37. Geological Society of America, 2007. doi: 10.1130/2007.2419(01).
- Johnson, G. R. Rock property measurements and analysis of selected igneous, sedimentary, and metamorphic rocks from worldwide localities. Report 2331-1258, USGS, 1983.
- Karato, S. Importance of anelasticity in the interpretation of seismic tomography. *Geophysical research letters*, 20(15): 1623–1626, 1993.
- Katayama, I., Terada, T., Okazaki, K., and Tanikawa, W. Episodic tremor and slow slip potentially linked to permeability contrasts at the Moho. *Nature Geoscience*, 5(10):731–734, 2012. doi: 10.1038/ngeo1559.
- Kjartansson, E. Constant Q-wave propagation and attenuation. *Journal of Geophysical Research*, 84(B9), 1979. doi: 10.1029/JB084iB09p04737.
- Kranz, R. L. Microcracks in rocks: A review. *Tectonophysics*, 100 (1-3):449–480, 1983. doi: 10.1016/0040-1951(83)90198-1.
- Lakes, R. *Viscoelastic Materials*. Cambridge University Press, 2009. doi: 10.1017/CBO9780511626722.
- Lee, T., Lakes, R. S., and Lal, A. Resonant ultrasound spectroscopy for measurement of mechanical damping: Comparison with broadband viscoelastic spectroscopy. *Review of Scientific Instruments*, 71(7):2855–2861, 2000. doi: 10.1063/1.1150703.
- Littel, G. F., Thomas, A. M., and Baltay, A. S. Using Tectonic Tremor to Constrain Seismic Wave Attenuation in Cascadia. *Geophysical Research Letters*, 45(18):9579–9587, 2018. doi: 10.1029/2018gl079344.
- Liu, H. P., Anderson, D. L., and Kanamori, H. Velocity dispersion due to anelasticity; implications for seismology and mantle composition. *Geophysical Journal International*, 47(1):41–58, 1976. doi: 10.1111/j.1365-246X.1976.tb01261.x.
- Madonna, C. and Tisato, N. A new Seismic Wave Attenuation Module to experimentally measure low-frequency attenuation in extensional mode. *Geophysical Prospecting*, 61(2):302–314, 2013. doi: 10.1111/1365-2478.12015.
- Mavko, G. and Nur, A. Melt squirt in the asthenosphere. *Journal of Geophysical Research*, 80(11):1444–1448, 1975. doi: 10.1029/JB080i011p01444.
- Mavko, G., Mukerji, T., and Dvorkin, J. *The Rock Physics Handbook*. Cambridge University Press, 3rd edition edition, 2020. doi: 10.1017/9781108333016.
- Mavko, G. M. and Nur, A. The effect of nonelliptical cracks on the compressibility of rocks. *Journal of Geophysical Research*, 83 (B9), 1978. doi: 10.1029/JB083iB09p04459.
- Mikhaltsevitch, V., Lebedev, M., Pervukhina, M., and Gurevich, B. Seismic dispersion and attenuation in Mancos shale – laboratory measurements. *Geophysical Prospecting*, 69(3):568–585, 2020. doi: 10.1111/1365-2478.13056.
- Muñoz-Montecinos, J., Angiboust, S., and Garcia-Casco, A. Blueschist-facies paleo-earthquakes in a serpentinite channel (Zagros suture, Iran) enlighten seismogenesis in Mariana-type subduction margins. *Earth and Planetary Science Letters*, 573, 2021. doi: 10.1016/j.epsl.2021.117135.
- Nakai, J. S., Sheehan, A. F., Abercrombie, R. E., and Eberhart-Phillips, D. Near Trench 3D Seismic Attenuation Offshore Northern Hikurangi Subduction Margin, North Island, New Zealand. *Journal of Geophysical Research: Solid Earth*, 126(3), 2021. doi: 10.1029/2020jb020810.
- Nowick, A. S. and Berry, B. S. *Anelastic Relaxation in Crystalline Solids*. Academic Press, 1972. doi: https://doi.org/10.1016/B978-0-12-522650-9.50005-7.
- Obana, K. and Kodaira, S. Low-frequency tremors associated with reverse faults in a shallow accretionary prism. *Earth and Planetary Science Letters*, 287(1-2):168–174, 2009. doi: 10.1016/j.epsl.2009.08.005.
- Obara, K. Nonvolcanic deep tremor associated with subduction in southwest Japan. *Science*, 296(5573):1679–81, 2002. doi: 10.1126/science.1070378.
- Obara, K. and Kato, A. Connecting slow earthquakes to huge earthquakes. *Science*, 353(6296):253–7, 2016. doi: 10.1126/science.aaf1512.
- Oberg, E. and McCauley, C. J. *Machinery's Handbook: Toolbox*. Industrial Press, Inc., 31st edition edition, 2020.
- O'Connell, R. J. and Budiansky, B. Seismic velocities in dry and saturated cracked solids. *Journal of Geophysical Research*, 79 (35):5412–5426, 1974. doi: 10.1029/JB079i035p05412.
- O'Connell, R. J. and Budiansky, B. Viscoelastic properties of fluid-saturated cracked solids. *Journal of Geophysical Research*, 82 (36):5719–5735, 1977. doi: 10.1029/JB082i036p05719.
- Peacock, S. M. Serpentinization and infiltration metasomatism in the Trinity peridotite, Klamath province, northern California: implications for subduction zones. *Contributions to Mineralogy and Petrology*, 95(1):55–70, 1987. doi: 10.1007/bf00518030.
- Philippot, P. and Selverstone, J. Trace-element-rich brines in eclogitic veins: implications for fluid composition and transport during subduction. *Contributions to Mineralogy and Petrology*, 106(4):417–430, 1991. doi: 10.1007/bf00321985.
- Pimienta, L., Fortin, J., and Guéguen, Y. Experimental study of Young's modulus dispersion and attenuation in fully saturated sandstones. *Geophysics*, 80(5):L57–L72, 2015. doi: 10.1190/geo2014-0532.1.
- Pimienta, L., Borgomano, J. V. M., Fortin, J., and Guéguen, Y. Modelling the drained/undrained transition: effect of the measuring method and the boundary conditions. *Geophysical Prospecting*, 64(4):1098–1111, 2016a. doi: 10.1111/1365-2478.12390.
- Pimienta, L., Fortin, J., and Guéguen, Y. Effect of fluids and frequencies on Poisson's ratio of sandstone samples. *Geophysics*, 81(2):D183–D195, 2016b. doi: 10.1190/GEO2015-0310.1.
- Pimienta, L., Borgomano, J. V. M., Fortin, J., and Guéguen, Y. Elastic Dispersion and Attenuation in Fully Saturated Sandstones: Role of Mineral Content, Porosity, and Pressures. *Journal of Geophysical Research: Solid Earth*, 122(12):9950–9965, 2017. doi: 10.1002/2017jb014645.
- Pimienta, L., Quintal, B., and Caspari, E. Hydro-mechanical coupling in porous rocks: hidden dependences to the microstructure? *Geophysical Journal International*, 224(2):973–984, 2021. doi: 10.1093/gji/ggaa497.
- Platt, J. P., Xia, H., and Schmidt, W. L. Rheology and stress in subduction zones around the aseismic/seismic transition. *Progress in Earth and Planetary Science*, 5(1), 2018. doi: 10.1186/s40645-018-0183-8.
- Pride, S. R., Berryman, J. G., and Harris, J. M. Seismic attenuation due to wave-induced flow. *Journal of Geophysical Research: Solid Earth*, 109(B1), 2004. doi: 10.1029/2003jb002639.
- Rorheim, S. On Frequency-Dependent Rock Experiments: A Comparative Review. *arXiv*, 2022. doi: https://doi.org/10.48550/arXiv.2208.03795.
- Saltiel, S., Selvadurai, P. A., Bonner, B. P., Glaser, S. D., and Ajo-Franklin, J. B. Experimental development of low-frequency shear modulus and attenuation measurements in mated rock fractures: Shear mechanics due to asperity contact area changes with normal stress. *Geophysics*, 82(2):M19–M36, 2017. doi: 10.1190/geo2016-0199.1.
- Sammis, C. G. and Bostock, M. G. A Granular Jamming Model for

- Low-Frequency Earthquakes. *Journal of Geophysical Research: Solid Earth*, 126(7), 2021. doi: 10.1029/2021jb021963.
- Schmitt, L., Forsans, T., and Santarelli, F. J. Shale testing and capillary phenomena. *International Journal of Rock Mechanics and Mining Sciences & Geomechanics Abstracts*, 31(5):411–427, 1994. doi: 10.1016/0148-9062(94)90145-7.
- Shapiro, N. M., Campillo, M., Kaminski, E., Vilotte, J., and Jaupart, C. Low-Frequency Earthquakes and Pore Pressure Transients in Subduction Zones. *Geophysical Research Letters*, 45(20), 2018. doi: 10.1029/2018gl079893.
- Shelly, D. R., Beroza, G. C., Ide, S., and Nakamura, S. Low-frequency earthquakes in Shikoku, Japan, and their relationship to episodic tremor and slip. *Nature*, 442(7099):188–91, 2006. doi: 10.1038/nature04931.
- Shelly, D. R., Beroza, G. C., and Ide, S. Non-volcanic tremor and low-frequency earthquake swarms. *Nature*, 446(7133):305–7, 2007. doi: 10.1038/nature05666.
- Spencer, J. W. Stress relaxations at low frequencies in fluid-saturated rocks: Attenuation and modulus dispersion. *Journal of Geophysical Research*, 86(B3), 1981. doi: 10.1029/JB086iB03p01803.
- Subramaniyan, S., Quintal, B., Tisato, N., Saenger, E. H., and Madonna, C. An overview of laboratory apparatuses to measure seismic attenuation in reservoir rocks. *Geophysical Prospecting*, 62(6):1211–1223, 2014. doi: 10.1111/1365-2478.12171.
- Subramaniyan, S., Quintal, B., Madonna, C., and Saenger, E. H. Laboratory-based seismic attenuation in Fontainebleau sandstone: Evidence of squirt flow. *Journal of Geophysical Research: Solid Earth*, 120(11):7526–7535, 2015. doi: 10.1002/2015jb012290.
- Sun, C., Tang, G., Fortin, J., Borgomano, J. V. M., and Wang, S. Dispersion and Attenuation of Elastic Wave Velocities: Impact of Microstructure Heterogeneity and Local Measurements. *Journal of Geophysical Research: Solid Earth*, 125(12), 2020. doi: 10.1029/2020jb020132.
- Supino, M., Poiata, N., Festa, G., Vilotte, J. P., Satriano, C., and Obara, K. Self-similarity of low-frequency earthquakes. *Sci Rep*, 10(1):6523, 2020. doi: 10.1038/s41598-020-63584-6.
- Tanikawa, W. and Shimamoto, T. Comparison of Klinkenberg-corrected gas permeability and water permeability in sedimentary rocks. *International Journal of Rock Mechanics and Mining Sciences*, 46(2):229–238, 2009. doi: 10.1016/j.ijrmmms.2008.03.004.
- Terzaghi, K., Peck, R., and Mesri, G. *Soil Mechanics in Engineering Practice*. Wiley, 1996.
- Tewksbury-Christle, C. M., Behr, W. M., and Helper, M. A. Tracking Deep Sediment Underplating in a Fossil Subduction Margin: Implications for Interface Rheology and Mass and Volatile Recycling. *Geochem Geophys Geosyst*, 22(3):e2020GC009463, 2021. doi: 10.1029/2020GC009463.
- Thomas, A. M., Beroza, G. C., and Shelly, D. R. Constraints on the source parameters of low-frequency earthquakes on the San Andreas Fault. *Geophysical Research Letters*, 43(4):1464–1471, 2016. doi: 10.1002/2015gl067173.
- Tisato, N. and Madonna, C. Attenuation at low seismic frequencies in partially saturated rocks: Measurements and description of a new apparatus. *Journal of Applied Geophysics*, 86:44–53, 2012. doi: 10.1016/j.jappgeo.2012.07.008.
- Tisato, N., Quintal, B., Chapman, S., Podladchikov, Y., and Burg, J. Bubbles attenuate elastic waves at seismic frequencies: First experimental evidence. *Geophysical Research Letters*, 42(10):3880–3887, 2015. doi: 10.1002/2015gl063538.
- Toksöz, M. N., Johnston, D. H., and Timur, A. Attenuation of seismic waves in dry and saturated rocks: I. Laboratory measurements. *Geophysics*, 44(4):681–690, 1979. doi: 10.1190/1.1440969.
- Walsh, J. B. The effect of cracks on the compressibility of rock. *Journal of Geophysical Research*, 70(2):381–389, 1965. doi: 10.1029/JZ070i002p00381.
- Wei, X., Xu, J., Liu, Y., and Chen, X. The slow self-arresting nature of low-frequency earthquakes. *Nat Commun*, 12(1):5464, 2021. doi: 10.1038/s41467-021-25823-w.
- White, J. E. Computed Seismic Speeds and Attenuation in Rocks with Partial Gas Saturation. *Geophysics*, 40(2):224–232, 1975. doi: 10.1190/1.1440520.
- Winkler, K. and Nur, A. Pore fluids and seismic attenuation in rocks. *Geophysical Research Letters*, 6(1):1–4, 1979. doi: 10.1029/GL006i001p00001.
- Yin, H., Borgomano, J. V. M., Wang, S., Tiennot, M., Fortin, J., and Guéguen, Y. Fluid Substitution and Shear Weakening in Clay-Bearing Sandstone at Seismic Frequencies. *Journal of Geophysical Research: Solid Earth*, 124(2):1254–1272, 2019. doi: 10.1029/2018jb016241.
- Zener, C. M. and Siegel, S. Elasticity and Anelasticity of Metals. *The Journal of Physical and Colloid Chemistry*, 53(9):1468–1468, 1949. doi: 10.1021/j150474a017.
- Zoback, M. D. and Byerlee, J. D. The effect of microcrack dilatancy on the permeability of westerly granite. *Journal of Geophysical Research*, 80(5):752–755, 1975. doi: 10.1029/JB080i005p00752.

The article *Dispersive Elastic Moduli and Frequency-Dependent Attenuation due to Wave-Induced Fluid Flow in Metapelite* © 2024 by C. Fliedner is licensed under CC BY 4.0.